Seismic evidence for a mantle transition zone origin of the Wudalianchi and Halaha volcanoes in Northeast China

Wei Wei[1]*, James O. S. Hammond[2], Dapeng Zhao[3], Jiandong Xu[1], Qian Liu[4], Yaning Gu[1]

[1] Key Laboratory of Active Tectonics and Volcano, Institute of Geology, China Earthquake Administration, Beijing 100029, China

[2] Department of Earth and Planetary Sciences, Birkbeck, University of London, London, WC1E 7HX, UK

[3] Department of Geophysics, Tohoku University, Sendai 980-8578, Japan

[4] Beijing Applied Meteorology Institute, Beijing, 100029, China

*Corresponding author: Wei Wei (weiwei@ies.ac.cn)

Key Points:

Local-scale low-velocity anomalies exist directly beneath the Wudalianchi and Halaha volcanoes.

A detached lithosphere is revealed as a high-velocity anomaly above the 410-km discontinuity.

The delaminated lithosphere and related mantle upwelling may control the location of Cenozoic volcanism.

Abstract

There exists much debate about origins of cretaceous-present volcanism in northeast (NE) China. Here we present high-resolution seismic images of the upper mantle beneath NE China by inverting P-wave travel-time data recorded by two dense linear arrays. The inclusion of the new data set has greatly improved sampling of the upper mantle beneath the study region, providing tight constraint on the seismic structure under the intraplate Wudalianchi and Halaha volcanoes. Local-scale low P-wave velocity (low-Vp) anomalies are revealed in the shallow mantle beneath the two volcanoes, whereas a large-scale high-Vp zone is imaged in the mantle transition zone (MTZ). These new results suggest that the two volcanoes, though located at different sites above the stagnant Pacific slab in the MTZ, are likely related to the deep subduction and dehydration of the Pacific slab, possibly through hot and wet upwellings in the big mantle wedge (BMW) beneath Wudalianchi and through deeper hydrous upwelling related to slab avalanche beneath Halaha. Our results also reveal other striking features, such as high-Vp structures resting atop the 410 km discontinuity beneath the Great Xing'an Range and the Songliao Basin, which are attributed to detached continental lithosphere. The delamination most likely occurred in the Cretaceous, which induced widespread magmatism in NE China.

1. Introduction

From the viewpoint of regional tectonics, NE China is located at the eastern edge of the Central Asian Orogenic Belt (CAOB). The Siberian craton bounds this feature to the north and the Tarim and North China cratons present the limit to the south making the CAOB one of the largest accretionary orogens on Earth. The CAOB is considered to have formed by the closure of multiple oceans and amalgamation of terrains of different types, deriving from quite diverse sources (Dobretsov et al., 1995; Xiao et al., 2003). In the early Cretaceous, NE China experienced intensive extensional deformation, which was manifested by widespread volcanism (Wu et al., 2005; Zhang et al., 2010), metamorphic core complexes (e.g., Donskaya et al., 2008), and the development of a series of extensional basins including the Songliao Basin (SLB) (Meng, 2003). The Cretaceous magmatism in NE China was dominant in the Great Xing'an Range (GXR), and it also occurred widely in the SLB and the Jiamusi region (Meng, 2003; Wang et al., 2006; Zhang et al., 2010). The deep dynamic processes associated with the large-scale extension and volcanic activity are still not well understood. Several mechanisms have been proposed, such as mantle plumes (Deng et al., 1996), lithospheric delamination (e.g., Zhang et al., 2010), and westward subduction and rollback of the Paleo-Pacific plate (Wu et al., 2005).

Intraplate volcanism in NE China continued through the Cenozoic and is mainly distributed along the northern, western and eastern edges of the SLB (Figure 1) (Fan & Hooper, 1991; Liu et al., 2001). Among the ~600 Cenozoic volcanoes in NE China (Liu et al., 2001), the Holocene ones are located in the Changbaishan, Longgang, Jingpohu, Wudalianchi, Halaha and Abaga areas (Figure 1). Volcanic rocks in these areas are largely of alkali basalt composition with some tholeiites (Chen et al., 2007; Ho et al., 2013; Kuritani et al., 2011; Wang et al., 2017; Xu et al., 2012; Zhao & Fan, 2012). Geochemical studies suggest that these Holocene basalts are characterized by a mix between an asthenospheric mantle and EM1 (enriched mantle 1) (e.g., Xu et al., 2012), however, whether the EM1 signature originates from the sub-continental lithospheric mantle (SCLM) or the recycled sediments or oceanic crust in an ancient stagnant slab in the MTZ remains hotly debated (e.g., Zhang et al., 1995; Kuritani et al., 2011; Xu et al., 2012).

Seismic tomography has been widely used to study the mantle structure and constrain the origin of intraplate volcanoes. Previous studies show that the Changbaishan volcano is underlain by a significant low-velocity (low-V) anomaly extending to a depth of ~400 km (e.g., Lei & Zhao, 2005; Zhang et al., 2013a; Zhao & Tian, 2013). In the MTZ (410-660 km depths), most studies show a broad high-velocity (high-V) zone associated with the subducted Pacific slab (Huang & Zhao, 2006; Li & van der Hilst, 2010; Tao et al., 2018; Wei et al., 2012, 2015; Zhang et al., 2013a; Zhao et al., 2009; Zhao & Tian, 2013). Zhao et al. (2009) proposed that the Changbaishan volcano was caused by the hot and wet upwelling flow in a BMW above this stagnant slab. However, a recent teleseismic tomography study suggested that while the location of Changbaishan volcano is linked to the deep subduction, the volcanism is related to a hot upwelling of sub-slab materials rising through a gab in the subducted slab (Tang et al., 2014). However, this suggestion is not supported by more recent tomographic studies of NE Asia (e.g., Chen et al., 2017a; Takeuchi et al., 2014) and so the origin of Changbaishan volcano remains a topic of debate. Compared to the Changbaishan volcano, the mantle structure beneath other Holocene volcanoes in NE China has not been investigated until very recently. Based on seismic data recorded by the NECESSArray (NE China extended seismic array), results of surface-wave tomography indicate that continuous low-V anomalies are present in the crust and shallow mantle under the Abaga and Halaha volcanoes, which are interpreted as local asthenospheric upwelling from a return flow driven by downwelling beneath the SLB (Guo et al., 2016). However, these seismic images have a reliable resolution to ~200 km depth, meaning it is unclear if the low-V anomalies beneath these volcanoes extend to a greater depth.

The Wudalianchi volcano is an active volcano with its most recent eruption dated to 1719-1721 CE (Liu, 2001). Despite the inclusion of the NECESSArray data, the fact that the station spacing in this region is ~70 km means the mantle structure under this volcano remains poorly constrained (Guo et al., 2016). A denser spacing of seismic stations is required to successfully image the localized distribution of volcanic rocks and the likely associated local melting source of the Wudalianchi volcano.

In this work, we have determined high-resolution tomographic images along two densely distributed linear arrays that span different tectonic units in NE China. In particular, one of the arrays passed through the Wudalianchi volcano, while the other array passed through the Halaha volcanic area (Figure 2). Our present results provide new constraints on the mantle structure beneath the Wudalianchi and Halaha intraplate volcanoes, allowing us to infer their origins and the mantle dynamics in NE China.

2. Data

Two linear, roughly parallel, NW-SE seismic arrays were deployed in NE China during April 2009 to September 2011 (Qiang & Wu, 2015; Zhang et al., 2013a, b). They consisted of 116 three-component broadband seismic stations. The profiles traversed (from west to east) the GXR, the SLB and the Jiamusi block. The total length of each array is ~1200 km, along which seismic stations were closely spaced at an average interval of ~20 km (Figure 2). Following the previous studies (Zhang et al., 2013b), hereafter we call the northern and southern profiles as EH and SM lines, respectively.

We selected seismograms from earthquakes with Ms ≥ 5.5 and epicentral distances of 30° to 95° (Figure 2). Considering the linear distribution of the seismic arrays, we only used earthquakes with back-azimuths very close (no more than 20°) to the strike of the EH and SM lines (Figure 2). With this criterion, we have collected a total of 2420 and 3661 P-wave arrival times from 63 and 87 earthquakes recorded by the EH and SM arrays, respectively. The teleseismic P waveforms are first filtered between 0.4 and 1.5 Hz, and then a multi-channel cross-correlation technique (VanDecar & Crosson, 1990) is applied to determine P-wave relative travel times across each profile, with a minimum cross-correlation coefficient of 0.85 and a mean root-mean-square (RMS) uncertainty of 0.02 s for the relative arrival times. To demonstrate what lateral extent of the Earth is sampled along the EH and SM lines, we show the piercing points of teleseismic rays at 100-600 km depths in Figures S1 and S2. For the P-wave data with the dominant period of 1 s, the Fresnel zone widths at 200 and 600 km depth are ~40 and 75 km, respectively. From Figures S1 and S2, it is clear that the sampling zones of seismic rays between EH and SM lines differ from each other in the shallow mantle (above 400-km depth), even considering the effect of P-wave Fresnel zone widths at each depth, suggesting that seismic structure below each line can be well distinguished by the data sets used in this study.

Our models have significantly improved the tomographic resolution compared to previous models for several reasons. First and foremost, the average station spacing of ~20 km means we have good crossing rays in the upper mantle, providing a better constraint on the size, location and depth extension of the anomalous structure beneath the volcanoes. Secondly, we only use the teleseismic events whose back-azimuths are close to the strike of EH and SM lines to avoid mapping the heterogeneous structures far from each line. Finally, because of the steep incident angles of teleseismic rays and their arriving at similar back-azimuths, the contribution of azimuthal anisotropy to the relative travel-time residuals is not evident, greatly reducing the tradeoff between the isotropic and azimuthal anisotropy velocity structures (e.g., Huang et al., 2014; Wei et al., 2015). O'Driscoll et al (2011) used SKS splitting parameters and the calculated P and S wave velocities along the wave propagation direction in a hexagonal anisotropic medium to estimate the effect of azimuthal anisotropy on telesesmic P-wave delays. They found that for a vertically arriving P-wave ray, it would cause 0.38 s P-wave delay when the observed SKS splitting time was 1 s. In this study, because we use seismic rays with similar back-azimuths and the relative travel-time (RTT) residuals in the inversion, the contribution of azimuthal anisotropy to the RTT residuals is less than 0.1 s

(O'Driscoll et al., 2011), considering that the overall observed SKS splitting times are of low amplitude (~0.8 s) in NE China (Li & Niu, 2010; Huang et al., 2011). This suggests that the effect of azimuthal anisotropy to the RTT residuals is small. The RTT residuals can also be affected by anisotropy if vertical flow is dominant in the upper mantle. If local-scale vertical flow aligns the olivine a-axis in a vertical orientation in the upper mantle along the EH and SM lines, it will cause the P waves to arrive relatively early, resulting in faster velocities in our tomography. This would imply that the amplitude of any low-Vp anomaly is underestimated or a high-Vp anomaly is overestimated. In NE China, ongoing lithospheric delamination has been inferred from a complicated anisotropic structure beneath the southern GXR and southwest SLB (Chen et al., 2017b), particularly due to extensive null splitting (Li et al., 2017) in these regions from shear wave splitting studies. However, in the northern GXR and the SLB (the focus of this paper), current mantle flow in a vertical direction is not evident or only exists very locally (Chen et al., 2017b; Li et al., 2017; Qiang & Wu, 2015), so the effect of vertical anisotropy on the RTT residuals is likely minimal. There is no evidence for the existence of the tilted anisotropy in the upper mantle of NE China. If it exists, its effect on the P-wave travel times is more complicated. At this stage, it is hard to investigate how much of the RTT residuals is caused by tilted anisotropy.

3. Method

3.1 Model parameterization and inversion

We used the tomographic method of Zhao et al. (2012) to invert the teleseismic data. We use a 3-D grid to parameterize our 3-D modeling space from 40°N to 55°N latitude, 113°E to 142°E longitude, with a lateral grid interval of 0.2° and from the surface to 900 km depth with a vertical grid interval of 20 km. The P-wave velocity (Vp) at each grid is calculated from the ak135 model (Kennett et al., 1995). A 3-D ray tracing technique (Zhao et al., 1992) is used to calculate theoretical travel times and ray paths, from which the RTT residuals are calculated (Zhao et al., 1994) and then used in the tomographic inversion.

The system of observation equations can be written as:

$$\boldsymbol{d} = \boldsymbol{G}\boldsymbol{m} \quad (1)$$

where $\boldsymbol{d}$ is the data vector consisting of the RTT residuals, $\boldsymbol{G}$ is a matrix consisting of travel-time partial derivatives representing the sampling by the rays at the 3-D grid nodes, and $\boldsymbol{m}$ is the unknown-parameter vector consisting of Vp perturbations at the grid nodes. To regularize this under-determined inverse problem we apply the LSQR algorithm (Paige & Saunders, 1982) with norm λ and gradient damping μ (for smoothing), to solve equation (1) by minimizing (Wei et al., 2013):

$$\|G.m - d\|^2 + \lambda^2 \|m\|^2 + \mu^2 \|L.m\|^2 \quad (2)$$

where L is the gradient operator.

3.2 Crustal correction

In teleseismic tomography, seismic rays arrive at stations with near-vertical incident angles and so resolution in the crust is poor. To avoid mapping the crustal anomalies into the upper mantle, causing systematic errors in the inverted results (e.g., Waldhauser et al., 2002), we conducted crustal correction to the RTT residuals before tomographic inversion. We use the CRUST1.0 model (Laske et al., 2013) and estimate the travel time of the crustal part of each ray through this model, which is subtracted from the observed arrival time. We then analyze the ray path and its corresponding travel time of each ray from the bottom of the 3-D crust to the bottom of the modeling space. This means that we only resolve the 3-D Vp structure in the mantle. Figure S3 shows the distribution of mean RTT residuals at stations of the EH and SM lines before the crustal correction. Figure 3 shows the ray paths and their corresponding RTT residuals along the EH and SM lines after the crustal correction. The mean RTT residuals at all the stations are also shown. It is evident that seismic rays cross well to at least 600 km depth (Figure 3). Comparing Figure 3b with Figure S3, we find that the mean RTT residuals are markedly reduced at the stations located in the SLB (SM line). This is expected because Vp in the thick sedimentary layer of the SLB would be much lower than those in the surrounding areas. This means that the RTT residuals at some stations in the SLB change from being relatively late arrivals to early ones after the crustal correction.

3.3 Regularization parameter selection

In this study, we take the same value for l and m in a range of 5 to 100 to investigate their effects on the final solution. We find that the data-variance reduction and variance of Vp perturbations from different damping and smoothing values can be represented by a trade-off curve. Following Eberhart-Philips (1986), we obtain the optimal damping and smoothing values through balancing the reduction of data variance with the requirement of producing a smooth 3-D Vp model. Tomographic models along the EH and SM lines are inverted separately, with the optimal damping and smoothing values of 15 and 20 for the EH and SM lines, respectively (Figure 4). The P-wave RMS RTT residuals before and after the inversion are 0.3613 and 0.1419 s for the EH line, and 0.4228 and 0.1415 s for the SM line, respectively (Figure 5). The variance reduction of the RTT residuals is 65% (from 0.1306 to 0.0457 s^2) for the EH line and 88.8% (from 0.1788 to 0.02 s^2) for the SM line (Figure 5).

4. Resolution analyses

To investigate the limitations of the data and the inversion method, we performed checkerboard resolution tests (CRTs). We first construct an input model containing spherical anomalies with alternating positive and negative Vp perturbations (+/-4%). The anomalies have a diameter of 70 km in the areas just south of the EH and SM lines. Synthetic travel times for the checkerboard model are calculated using the same source-receiver geometries as those in our data set. Random noise with a standard deviation of 0.1 s is added to the synthetic travel times to simulate the observation errors in the real data. The synthetic dataset is then inverted using the same methods, parameterization and regularization as for the real data inversion. The recovered images of the checkerboard model (Figures S4 and S5) then give an indication of which parts of our model are most reliable. The CRT results show that resolution is good in the upper mantle beneath both the EH and SM lines (Figures S4 and S5). In the MTZ and lower mantle, the input patterns of Vp anomalies can also be recovered, however, significant vertical smearing occurs along the steeply inclined ray paths at those depths (Figures S4 and S5). The CRT results suggest that the input anomalies can be resolved with an amplitude recovery rate of ~40-50%. A recent study suggests that, compared to the conventional tightly spaced CRTs, the discrete spike tests can better reveal the resolving power of a data set and the direction of smearing in the inverted solution (Rawlinson & Spakman, 2016). We conducted the discrete spike tests with different scale lengths of structure (Figures 6, 7, S6 and S7), which indicate that the large-scale structure (spherical anomaly with a Gaussian width of 50 km) is better retrieved than the fine-scale one (spherical anomaly with a Gaussian width of 35 km) for both the EH and SM lines. These resolution tests suggest that our high-quality datasets are able to resolve structural features on the order of 50 km length scales to a depth of at least 400 km (Figures 6, 7, S4 and S5) and larger structures to greater depths.

4. Results

Figures 8 and 9 show map views of Vp tomography from our inversions of the RTT residual data recorded at stations along the EH and SM lines, respectively. Because most of the teleseismic events used are located in slightly more southern azimuths relative to the orientation of the EH and SM lines (Figure 2), seismic rays mainly sample the zones just south of each line in the upper mantle (Figures S1 and S2), and this is why the deep structure of the Halaha volcano, although located to the south of the SM line, can be well resolved (Figures 7 and 9). Our results show that there is no significant Vp variation in the NE-SW direction along each line, i.e., normal to the strike of the EH and SM lines (Figures 8 and 9). This is expected, because we only used the teleseismic events which are located within 20° to the strike of the EH and SM lines. The tomographic results mainly reflect the dominant structure around each line. In addition, the trend of major geologic structures in NE China is NE-SW oriented (Figure 1), and so we expect that the mantle structure in the region may not change much in the NE-SW direction at least at the scale of the tomographic resolution (~50 km). Therefore, our tomographic results can be best represented by vertical cross-sections along the EH and SM lines (Figure 10).

A low-Vp anomaly with a width of ~80 km is evident directly beneath the Wudalianchi volcano (Figure 10a). It extends from the depth of ~35 km to ~200 km and is further elongated southeastwards to 400 km depth. A spatially continuous high-Vp anomaly is present in the MTZ under the Wudalianchi volcanic area and its western part extends down to the lower mantle. Considering the previous results of regional and global tomography (e.g., Fukao et al., 2009; Huang & Zhao, 2006; Li & van der Hilst, 2010; Obayashi et al., 2013; Wei et al., 2012, 2015; Zhao, 2004; Zhao et al., 2013), we suggest that the high-Vp anomaly delineates the current location of the subducted Pacific slab. Another high-Vp zone is present at depths of ~300-500 km in the western part of the EH profile, directly beneath and to the southeast of the GXR (Figure 10a). The two high-Vp anomalies seem to connect in the MTZ.

Our model below the SM line shows a broadly inclined low-Vp anomaly beneath the GXR (Figure 10b). It is deeply rooted in the MTZ and continuously extends to the shallow mantle (~120 km depth), where it spreads laterally to a much larger area. A smaller low-Vp anomaly is located directly beneath the Halaha volcano and seems to connect with the large-scale low-Vp body (Figure 10b). Beneath the SLB, the model shows a large low-Vp anomaly in the shallow mantle underlain by a high-Vp layer with a thickness of ~100 km. In the MTZ and lower mantle, a large high-Vp anomaly is imaged, which is similar to the feature in the EH line, corresponding to the subducted Pacific slab.

While the checkerboard tests give a good indication of the resolution of our models, they represent non-geological structures. To better understand the ability of the inversion to image the main features we interpret, we carried out more realistic synthetic tests. We generate a synthetic input model with a large slab structure in the MTZ and smaller, local upwelling in the upper mantle. We calculate synthetic travel times for the input model and perform a tomographic inversion using the same approach as described for the CRTs. The test results (Figure 11) show that the main features we interpret here are well resolved, though some vertical smearing occurs in the MTZ and lower mantle.

Figure S8 show tomographic results along the EH and SM lines without the crustal correction. By comparing Figure S8 with Figure 10, it is clear that there is no significant difference in the tomographic images at depths greater than 100 km. We also jointly inverted the RTT residuals from the EH and SM lines. The main features resolved (Figure S9) are generally consistent with the results achieved by the separate inversions of the seismic data from each line (Figure 10). In addition, we have conducted a tomographic inversion with our previous regional model (Wei et al., 2012) as a 3-D starting model. It should be noted that the previous model poorly constrains the upper mantle structure beneath the EH and SM lines (Figure S10) because of the lack of digital seismic stations in NE China. The inversion results are shown in Figure S11. Although there are some variations in the images in the very shallow mantle compared to the results shown in Figure 10, the main results that discussed in the text remain the same.

5. Discussion

4.1 Origin of the Wudalianchi volcano

The origin of the Wudalianchi volcano is the target of many geophysical and geochemical studies (Chen et al., 2007; Kuritani et al., 2013; Wang et al., 2017; Wei et al., 2012; Zhang et al., 1995, 2013a; Zhao, 2004; Zou et al., 2003). Its unceratainty is partly due to a lack of high-resolution seismic images of the mantle structure beneath the volcano. It is debated whether the Wudalianchi volcanism is related to hot and wet upwelling flow within the BMW (Zhao, 2004; Zhao et al., 2013) or a result of shallower processes (e.g., Zhang et al., 1998). Our new model (Figure 10a) shows a narrow, vertically continuous low-Vp anomaly beneath the Wudalianchi volcano, which extends to a depth of 200 km, and then oblique to the direction of SE to a depth of 400 km. In the MTZ, a large-scale high-Vp structure is revealed (Figure 10a), which represents the subducting Pacific slab. While we cannot rule out a connection of this low-Vp material to deeper structure in the SW-NE direction, our tomographic result suggests that the Wudalianchi volcano is very likely associated with the stagnant Pacific slab (Figure 10a).

Experimental studies show that in the MTZ wadsleyite and ringwoodite can carry significant amounts of water (2-3 wt%) (e.g., Kohlstedt et al., 1996; Smyth, 1987). This is more than olivine in the upper mantle and perovskite and magnesiowüstite in the lower mantle can carry (e.g., Ohtani et al., 2004), suggesting that the MTZ may be an important water reservoir in deep-Earth fluid cycling (e.g., Bercovici & Karato, 2003; Karato, 2011; Maruyama & Okamoto, 2007). A high water content in the MTZ beneath NE China has been suggested by a series of geochemical and geophysical studies (e.g., Ichiki et al., 2001; Kelbert et al., 2009; Wang et al., 2015). In particular, a recent seismological study suggests that the water content is ~0.2-0.4 wt% in the MTZ beneath NE China, but in some areas where the Pacific slab is thought to exist, the water content may be as high as 0.8 wt % (Wei et al., 2015). This suggests that a wet MTZ may exist beneath the study region. This result is supported by the existence of a high-conductivity anomaly in the MTZ beneath NE China (Guo & Yoshino, 2013; Ichiki et al., 2001; Kelbert et al., 2009), which is considered to be caused by the release of water from the stagnant Pacific slab. In addition, it has been suggested that as the slab is very old and therefore cold, hydrous phases in the slab are stable to depths greater than 410 km and that dehydration reactions may occur in the slab at MTZ depths (e.g., Kuritani et al., 2011, 2013; Ohtani et al., 2004; Ohtani & Zhao, 2009).

Many researchers have used these results to infer that deep dehydration of the slab leads to buoyant, hydrous upwelling that can facilitate melting, leading to the present-day intraplate volcanism in NE China, particularly at Changbaishan (Chen et al., 2017a; Lei & Zhao, 2005; Ma et al., 2018; Tian et al., 2016; Wei et al., 2015; Zhang et al., 2013a; Zhao et al., 2009). Our present tomographic results show that this is a plausible mechanism driving volcanism at Wudalianchi, where a local upwelling exists above the stagnant Pacific slab. This is similar to the result obtained by high-resolution local tomography beneath the Changbaishan volcano (Zhao & Tian, 2013). A geochemical study of the Wudalianchi volcano shows prominent positive spikes for Ba, Pb and Sr in potassic basalts (Wang et al., 2017), which are typical for hydrated mantle melts (Barry et al., 2007; Sakuyama et al., 2013; Wang et al., 2015). Results of numerical modeling indicate that Rayleigh-Taylor type instabilities could be triggered at the top of the stagnant Pacific slab due to its being heated from above (Richard & Bercovici, 2009). The upwelling wet plumes would release their water and induce partial melting atop the 410-km discontinuity, forming a water saturated melt layer (Bercovici & Karato, 2003). A recent seismological study indeed found an apparent low-velocity layer atop the 410-km discontinuity beneath NE China (Tauzin et al., 2017), which reinforced the conclusion of the convective dehydration of the stagnant slab in the region. The wet upwelling would further go up to the shallow mantle to drive the intraplate volcanism at Wudalianchi.

4.2 Origin of the Halaha volcano

Numerical models suggest that a focused upwelling can be produced at the leading edge of a subducting slab in the back arc, which may cause volcanism far from the trench (Faccenna et al., 2010). This atypical plume-like structure is revealed by mantle tomography in the western US (Li et al., 2008) and the Mediterranean region (Piromallo & Morelli, 2003). In NE China, previous tomographic studies have shown that the leading edge of the stagnant Pacific slab in the MTZ reaches the eastern margin of the GXR, close to the Halaha volcanic field (e.g., Huang & Zhao, 2006; Li & van der Hilst, 2010; Obayashi et al., 2013; Wei et al., 2012). Here a question arises: does the Halaha volcanism belong to this type or is it related to the stagnant Pacific slab itself?

Our new tomographic results demonstrate that a large high-Vp anomaly corresponding to the Pacific slab is present in the MTZ beneath NE China (Figure 10). Its western part, however, has likely descended to the lower mantle. It should be noted that this structure could be affected by vertical smearing (Figure S5), due to the limited crossing rays in the lower mantle (Figure 3b). Global tomography and other seismological investigations have revealed that the stagnant slab in this region eventually descends into the lower mantle through a slab avalanche (e.g., Fukao et al., 2009; Li et al., 2008; Zhao, 2004). When this occurs, most water in the slab will be released through dehydration melting at the top of the lower mantle (Schmandt et al., 2014), generating slightly buoyant hydrous melt that would rise, returning water to the MTZ (Schmandt et al., 2014). We invoke this mechanism to explain the pronounced low-Vp anomaly in our new model just above the westernmost part of the subducted Pacific slab (Figure 10b). It continuously extends upward from ~500 km depth to the shallow mantle at ~120 km depth, where it appears to spread laterally (Figure 10b), although our model has a lower resolution off the profile.

The lithospheric thickness beneath the GXR is estimated to be 140~160 km from S-wave receiver functions (Zhang et al., 2014) and ~120 km by magnetotelluric sounding (Liu et al., 2006). The laterally extensive low-Vp anomaly imaged at depths of ~120-200 km is possibly due to the impingement of a large-scale upwelling with the rigid lithosphere. We find a localized low-Vp anomaly with a width of ~80 km right beneath the Halaha volcano. It appears to be connected with the large-scale low-Vp anomaly in the asthenosphere and extends vertically through the lithosphere (Figure 10b). The present results indicate that the recent volcanism is not located directly above the large-scale upwelling plume but rather, is ~200 km away. A similar structure is imaged beneath an intraplate volcano in Khanuy Gol, central Mongolia (Zhang et al., 2017). They suggest that the upwelling is possibly related to the subduction of the Indian plate into deep mantle beneath the Mongolia. Geochemical studies have suggested that the Halaha basalts are characterized by lower $^{87}Sr/^{86}Sr$ and higher $^{143}Nd/^{144}Nd$ ratios than average, suggesting that the asthenosphere in this region is depleted (Ho et al., 2013; Zhao & Fan, 2012). In addition, the rare earth element (REE) and trace element patterns are similar to those of ocean island basalts, suggesting that their source zones are metasomatized by fluids from a relatively deep area (Zhao & Fan, 2012). Based on our new tomographic images, we suggest that the source of the fluids is the MTZ. We speculate that large-scale wet and hot upwelling from the MTZ may cause extension of the overlying lithosphere and the Halaha volcano may be a direct result of the local upwelling along lithospheric fractures or rifting.

4.3 Lithospheric delamination and its effect on cretaceous-present volcanism

During the Cretaceous, massive magmatism occurred in the GXR, the SLB and nearby regions of NE China. Results of petrologic and geochemical studies suggest that the large-scale volcanism in this period was caused by lithospheric delamination and subsequent asthenospheric upwelling (Wu et al., 2005; Zhang et al., 2010). Based on recent results of surface-wave tomography, Guo et al. (2015) argued that the lower crust may even have been removed in the delamination process. Our new models show a pronounced high-Vp anomaly at depths of ~300-500 km directly beneath and southeast of the GXR (Figure 10a). This feature was also revealed by our previous continental-scale tomographic study (Wei et al., 2012), which was interpreted as a delaminated lithosphere. However, the lack of evidence for large-scale vertical mantle flow at present beneath the northern GXR (Chen et al., 2017b; Huang et al., 2011) suggests that the delamination is more likely caused by old tectonic events that occurred , e.g., in the Cretaceous.

Along the SM line, a large low-Vp anomaly is present beneath the SLB and extends to ~200 km depth, which is underlain by a high-Vp layer with a thickness of ~100 km right above the 410-km discontinuity (Figure 10b). Considering the high heat flow with an average of 70.9 ± 14.4 mW.m^{-2} (Jiang et al., 2016) and high geothermal gradient with a maximum of 6.2°C/100 m measured in the SLB (Tian et al., 1992), it is reasonable to interpret this low-Vp zone as a hotter anomaly in the shallow mantle than the surrounding areas. Estimates of the lithosphere-asthenosphere boundary depth beneath NE China from an S-wave receiver-function study (Zhang et al., 2014) suggest that the lithospheric thickness beneath the SLB is ~100-120 km, significantly smaller than that under the GXR to the west (~140-160 km) and adjacent regions to the east (~120-150 km). The lithospheric thinning of the SLB has been reported by many previous studies (e.g., Meng et al., 2003; Ren et al., 2002), but its dynamic mechanism has long been a topic of debate. Our present results suggest that it is most likely caused by lithospheric delamination. The detached lithosphere is now located below the SLB and above the 410-discontinuity, which is imaged as a high-Vp structure (Figure 10b). A recent study indicates that the detached lithosphere can remain intact after delamination for more than 50 Ma (Bao et al., 2014). Following previous studies (Wu et al., 2005; Zhang et al., 2010), we suggest that the delamination occurred in the Cretaceous, then upwelling of the asthenosphere caused the large-scale volcanism around the SLB.

Our results indicate that the detached lithosphere beneath the GXR seems to pass through the 410-discontinuity and drop down to the MTZ, while the detached lithosphere beneath the SLB is still located above the 410-discontinuity (Figure 10a and b). If the same falling velocity is assumed, the large-scale lithospheric delamination should occur with a trend from the west to the east, which is consistent with the eastward decrease in age of the Cretaceous volcanic rocks (Zhang et al., 2010). We suggest that the subduction and rollback of the Paleo-Pacific plate may have played an important role in controlling the lithospheric delamination migrating eastward in the Cretaceous. The delamination resulted in the upwelling of the asthenosphere, which induced the extensive volcanism in NE China in the Cretaceous.

This sinking continental lithosphere may also play a role in the current volcanism. Recent shear-wave splitting studies show evidence for extensive null splitting in the SLB and surrounding regions, suggesting the existence of vertical mantle flow (Chen et al., 2017b; Li et al., 2017). This can be explained by the sinking of the delaminated lithosphere with return flow around the edges. Interestingly, the Cenozoic volcanism is located around the edges of the SLB (Figure 1). We suggest that the return flow from the sinking lithosphere could cause thermal anomalies responsible for the Cenozoic volcanism at some volcanoes in NE China. However, we see the low-Vp anomaly extending to 500 km and 400 km depth beneath the Halaha and Wudalianchi volcanoes, respectively, suggesting deeper processes are involved, but the delaminated lithosphere may still control the location of volcanism because upwelling material would need to flow around it.

6. Conclusions

In this study, high-resolution P-wave velocity images beneath NE China are obtained by inverting teleseismic P-wave data recorded by two dense linear arrays. Our results reveal more details of the mantle structure and origin of the Wudalianchi and Halaha intraplate volcanoes, which are of great importance for better understanding the volcanism and mantle dynamics of NE China.

Our results indicate that the deep subduction of the Pacific plate has affected the formation of both of the volcanoes. A large-scale high-Vp anomaly is revealed in the MTZ and uppermost lower mantle beneath the Wudalianchi volcano, above which a smaller-scale low-Vp structure exists in the upper mantle These results suggest that the formation of the Wudalianchi volcano is associated with the upwelling of wet and hot asthenospheric materials in the BMW above the stagnant Pacific slab in the MTZ (Figure 12). The Halaha volcano is located immediately above the western edge of the subducted Pacific slab. Our new results show that the Halaha volcano is fed by a localized upwelling, similar to the Wudalianchi volcano. But their difference is that the Halaha volcano is connected with a broad low-Vp structure to a depth of ~500 km. We suggest that the Halaha volcano is related to a focused upwelling produced by the falling down of the subducted Pacific slab into the lower mantle (Figure 12).

Some high-Vp structures on and around the 410-km discontinuity are revealed beneath the GXR and SLB, which may reflect the detached lithosphere. The lithospheric delamination most likely occurred in the Cretaceous and caused widespread volcanism of NE China in that period and may partly control the location of the intraplate volcanism today.

Acknowledgements

We thank Prof. Qingju Wu and other members who took part in the field work for deploying the seismometers and collecting the data. The waveform data were provided by the China Seismic Array Data Management Center at Institute of Geophysics, China Earthquake Administration. The data can be accessed either from the data center (http://www.chinarraydmc.cn) or directly from the corresponding author (W. Wei) via Email. This work was supported by grants from the Chinese NSFC (41604042, 41874110) to W. Wei and a grant from MEXT (No. 26106005) to D. Zhao. Most figures were made using the Generic Mapping Tools (Wessel et al., 2013). Prof. Maureen Long (the Editor), Prof. Brian Savage and an anonymous referee provided thoughtful comments and suggestions that have improved this paper.

References

Bao, X., Eaton, D. W., & Guest, B. (2014). Plateau uplift in western Canada caused by lithospheric delamination along a craton edge. *Nature Geoscience*, 7, 830-833.

Barry, T. L., Ivanov, A. V., Rasskazov, S. V., Demonterova, E. I., Dunai, T. J., Davies, G. R., & Harrison, D. (2007). Helium isotopes provide no evidence for deep mantle involvement in widespread Cenozoic volcanism across Central Asia. *Lithos*, 95, 415-424.

Bercovici, D., & Karato, S. (2003). Whole-mantle convection and the transition-zone water filter. *Nature*, 425, 39-44.

Chen, C., Zhao, D., Tian, Y., Wu, S., Hasegawa, A., Lei, J., Park, J., & Kang, I. (2017a). Mantle transition zone, stagnant slab and intraplate volcanism in Northeast Asia. *Geophysical Journal International*, 209, 68-85.

Chen, H., Niu, F., Obayashi, M., Grand, P., Kawakatsu, H., Chen, Y., Ning, J., & Tanaka, S. (2017b). Mantle seismic anisotropy beneath NE China and implications for the lithospheric delamination hypothesis beneath the southern Great Xing'an range. *Earth and Planetary Science Letters*, 471, 32-41.

Chen, Y., Zhang, Y., Graham, D., Su, S., & Deng, J. (2007). Geochemistry of Cenozoic basalts and mantle xenoliths in Northeast China. *Lithos*, 96, 108-126.

ChinArray. (2006). China Seismic Array waveform data. China Earthquake Administration. https://doi:10.12001/ChinArray.Data.

Deng, J. F., Zhao, H. L., Mo, X. X., Luo, Z. H., & Du, S. Y. (1996). Continental root/plume structure in China - key to the continental geodynamics. Geological Publishing House, Beijing, pp. 1 － 110.

Dobretsov, N. L., Berzin, N. A., & Buslov, M. M. (1995). Opening and tectonic evolution of the Paleo-Asian Ocean. *International Geology Review*, 37, 335-360.

Donskaya, T. V., Windley, B. F., Mazukabzov, A. M., Kroner, A., Sklyarov, E. V., Gladkochub, D. P., Ponomarchuk, V. A., Badarch, G., Reichow, M. K., & Hegner, E. (2008). Age and evolution of late Mesozoic metamorphic core complexes in southern Siberia and northern Mongolia. *Journal of the Geological Society, London*, 165, 405-421.

Eberhart-Phillips, D. (1986). Three-dimensional velocity structure in northern California Coast Ranges from inversion of local earthquake arrival times. *Bulletin of the Seismological Society of America*, 76, 1025-1052.

Faccenna, C., Becker, T. W., Lallemand, S., Lagabrielle, Y., Funiciello, F., & Piromallo, C. (2010). Subduction-triggered magmatic pulses: A new class of plumes?. *Earth and Planetary Science Letters*, 299, 54-68.

Fan, Q., & Hooper, P. R. (1991). The Cenozoic basaltic rocks of eastern China: petrology and chemical composition. *Journal of Petrology*, 32, 765-810.

Fukao, Y., Obayashi, M., Nakakuki, T., & the Deep Slab Project Group. (2009). Stagnant slab: a review. *Annual Review of Earth Planetary Sciences*, 37, 19-46.

Guo, X., & Yoshino, T. (2013). Electrical conductivity of dense hydrous magnesium silicates with implication for conductivity in the stagnant slab. *Earth and*

Planetary Science Letters, 369, 239-247.

Guo, Z., Chen, Y. J., Ning, J., Feng, Y., Grand, S. P., Niu, F., Kawakatsu, H., Tanaka, S., Obayashi, M., & Ni, J. (2015). High resolution 3-D crustal structure beneath NE China from joint inversion of ambient noise and receiver functions using NECESSArray data. *Earth and Planetary Science Letters*, 416, 1-11.

Guo, Z., Chen, Y. J., Ning, J., Yang, Y., Afonso, J. C., & Tang, Y. (2016). Seismic evidence of on-going sublithosphere upper mantle convection for intra-plate volcanism in Northeast China. *Earth and Planetary Science Letters*, 433, 31-43.

Ho, K., Ge, W., Chen, J., You, C., Yang, H., & Zhang, Y. (2013). Late Cenozoic magmatic transitions in the central Great Xing'an Range, Northeast China: Geochemical and isotopic constraints on petrogenesis. *Chemical Geology*, 352, 1-18.

Huang, J., & Zhao, D. (2006). High-resolution mantle tomography of China and surrounding regions. *Journal of Geophysical Research: Solid Earth*, 111, B09305, https://doi:10.1029/2005JB004066.

Huang, Z., Wang, L., Zhao, D., Mi, N., & Xu, M. (2011). Seismic anisotropy and mantle dynamics beneath China. *Earth and Planetary Science Letters*, 306, 105-117.

Huang, Z., Wang, P., Zhao, D., Wang, L., & M. Xu (2014). Three-dimensional P-wave azimuthal anisotropy in the lithosphere beneath China. *Journal of Geophysical Research: Solid Earth*, 119, 5686-5712.

Ichiki, M., Uyeshima, M., Utada, H., Guoze, Z., Ji, T., & M, M. (2001). Upper mantle conductivity structure of the back-arc region beneath northeastern China. *Geophysical Research Letters*, 28, 3773-3776.

Jiang, G., Gao, P., Rao, S., Zhang, L., Tang, X., Huang, F., Zhao, P., Pang, Z., He, L., Hu, S., & Wang, J. (2016). Compilation of heat flow data in the continental area of China (4^{th} edition). *Chinese Journal of Geophysics*, 59, 2892-2910 (in Chinese with English abstract).

Karato, S. (2011). Water distribution across the mantle transition zone and its implications for global material circulation. *Earth and Planetary Science Letters*, 301, 413-423.

Kelbert, A., Schultz, A., & Egbert, G. (2009). Global electromagnetic induction constraints on transition-zone water content variations. *Nature*, 460, 1003-1006.

Kennett, B., Engdahl, E., & Buland, R. (1995). Constraints on seismic velocities in the Earth from traveltimes. *Geophysical Journal International*, 122, 108-124.

Kohlstedt, D. L., Keppler, H., & Rubie, D. C. (1996). Solubility of water in the α, β and γ phases of $(Mg,Fe)_2SiO_4$. *Contributions to Mineralogy and Petrology*, 123, 345-357.

Kuritani, T., Ohtani, E., & Kimura, J. (2011). Intensive hydration of the mantle transition zone beneath China caused by ancient slab stagnation. *Nature Geoscience*, 4, 713-716.

Kuritani, T., Kimura, J., Ohtani, E., Miyamoto, H., & Furuyama, K. (2013). Transition zone origin of potassic basalts from Wudalianchi volcano, northeast China. *Lithos*, 156, 1-12.

Laske, G., Masters, G., Ma, Z., & Pasyanos, M. (2013). Update on CRUST1.0 – A 1-degree Global Model of Earth’s Crust. *Geophysical Research Abstracts*, 15, EGU2013-2658.

Lei, J., & Zhao, D. (2005). P-wave tomography and origin of the Changbai intraplate volcano in Northeast Asia. *Tectonophysics*, 397, 281-295.

Li, C., & Van Der Hilst, R. D. (2010). Structure of the upper mantle and transition zone beneath Southeast Asia from traveltime tomography. *Journal of Geophysical Research: Solid Earth*, 115, B07308, https://doi:10.1029/2009JB006882.

Li, C., Van der Hilst, R. D., Engdahl, E. R., & Burdick, S. (2008). A new global model for P wave speed variations in Earth's mantle. *Geochemistry Geophysics Geosystems*, 9, Q05018, https://doi:10.1029/2007GC001806.

Li, J., & Niu, F. (2010). Seismic anisotropy and mantle flow beneath northeast China inferred from regional seismic networks. *Journal of Geophysical Research: Solid Earth*, 115, doi:10.1029/2010JB007470.

Li, S., Guo, Z., & Chen, Y. (2017). Complicated 3D mantle flow beneath Northeast China from shear wave splitting and its implication for the Cenozoic intraplate volcanism. *Tectonophysics*, 709, 1-8.

Liu, G. X., Zhang, Z. H., Han, J. T., & Tang, J. H. (2006). Features of the electric structure of the lithosphere beneath the Hinggan–Inner Mongolia and Jilin–Heilongjiang regions. *Geology in China*, 33, 824–831 (in Chinese with English abstract).

Liu, J., Han, J., & Fyfe, W. S. (2001). Cenozoic episodic volcanism and continental rifting in northeast China and possible link to Japan Sea development as revealed from K-Ar geochronology. *Tectonophysics*, 339, 385-401.

Ma, J., Tian, Y., Liu, C., Zhao, D., Feng, X., & Zhu, H. (2018). P-wave tomography of Northeast Asia: Constraints on the western Pacific plate subduction and mantle dynamics. *Physics of the Earth and Planetary Interiors*, 274, 105-126.

Maruyama, S., & Okamoto, K. (2007). Water transportation from the subducting slab into the mantle transition zone. *Gondwana Research*, 11, 148-165.

Meng, Q. (2003). What drove late Mesozoic extension of the northern China-Mongolia tract?. *Tectonophysics*, 369, 155-174.

Obayashi, M., Yoshimitsu, J., Nolet, G., Fukao, Y., Shiobara, H., Sugioka, H., Miyamachi, H., & Gao, Y. (2013). Finite frequency whole mantle P wave tomography: Improvement of subducted slab images. *Geophysical Research Letters*, 40, 5652-5657.

O'Driscoll, L., Humphreys, E., & Schmandt, B. (2011), Time corrections to teleseismic P delays derived from SKS splitting parameters and implications for western U.S. P-wave tomography. *Geophysical Research Letters*, 38, L19304, doi:10.1029/2011GL049031.

Ohtani, E., Litasov, K., Hosoya, T., Kubo, T., & Kondo, T. (2004). Water transport into the deep mantle and formation of a hydrous transition zone. *Physics of the Earth and Planetary Interiors*, 143, 255-269.

Ohtani, E., & Zhao, D. (2009). The role of water in the deep upper mantle and transition zone: dehydration of stagnant slabs and its effects on the big mantle wedge. *Russian Geology and Geophysics*, 50, 1073-1078.

Paige, C. C., & Saunders, M. A. (1982). LSQR: An algorithm for sparse linear equations and sparse least squares. *ACM Transactions on Mathematical Software*, 8, 43-71.

Piromallo, C. & Morelli, A. (2003). P wave tomography of the mantle under the Alpine-Mediterranean area. *Journal of Geophysical Research: Solid Earth*, 108, B2, 2065, https://doi:10.1029/2002JB001757.

Qiang, Z., & Wu, Q. (2015). Upper mantle anisotropy beneath the north of northeast China and its dynamic significance. *Chinese Journal of Geophysics*, 58, 3540-3552 (in Chinese with English abstract).

Rawlinson, N., & Spakman, W. (2016). On the use of sensitivity tests in seismic tomography. *Geophysical Journal International*, 205, 1221-1243.

Ren, J., Tamaki, K., Li, S., & Junxia, Z. (2002). Late Mesozoic and Cenozoic rifting and its dynamic setting in Eastern China and adjacent areas. *Tectonophysics*, 344, 175-205.

Richard, G. C., & Bercovici, D. (2009). Water-induced convection in the Earth's mantle transition zone. *Journal of Geophysical Research: Solid Earth*, 114, doi:10.1029/2008JB005734.

Sakuyama, T., Tian, W., Kimura, J., Fukao, Y., Hirahara, Y., Takahashi, T., Senda, R., Chang, Q., Miyazaki, T., & Obayashi, M. (2013). Melting of dehydrated oceanic crust from the stagnant slab and of the hydrated mantle transition zone:

Constraints from Cenozoic alkaline basalts in eastern China. *Chemical Geology*, 359, 32-48.

Schmandt, B., Jacobsen, S. D., Becker, T. W., Liu, Z., & Dueker, K. G. (2014). Dehydration melting at the top of the lower mantle. *Science*, 344, 1265-1268.

Smyth, J. R. (1987). β-Mg2SiO4: A potential host for water in the mantle. *American Mineralogist*, 72, 1051-1055.

Takeuchi, N., Kawakatsu, H., Tanaka, S., Obayashi, M., Chen, Y. J., Ning, J., Grand, S. P., Niu, F., Ni, J., Iritani, R., Idehara, K., & Tonegawa, T. (2014). Upper mantle tomography in the northwestern Pacific region using triplicated P waves, *Journal of Geophysical Research: Solid Earth*, 119, 7667-7685.

Tang, Y., Obayashi, M., Niu, F., Grand, S. P., Chen, Y. J., Kawakatsu, H., Tanaka, S., Ning, J., & Ni, J. F. (2014). Changbaishan volcanism in northeast China linked to subduction-induced mantle upwelling. *Nature Geoscience*, 7, 470-475.

Tao, K., Grand, S. P., & Niu, F. (2018). Seismic structure of the upper mantle beneath Eastern Asia from full waveform seismic tomography. *Geochemistry Geophysics Geosystems*, 19, 2732-2763.

Tauzin, B., Kim, S., & Kennett, B. L. N. (2017). Pervasive seismic low-velocity zones within stagnant plates in the mantle transition zone: Thermal or compositional origin? *Earth and Planetary Science Letters*, 477, 1-13.

Tian, Y., Zhu, H., Zhao, D., Liu, C., Feng, X., Liu, T., & Ma, J. (2016). Mantle transition zone structure beneath the Changbai volcano: Insight into deep slab dehydration and hot upwelling near the 410-km discontinuity. *Journal of*

Geophysical Research: Solid Earth, 121, 5794-5808.

Tian, Z., Han, P., & Xu, K. (1992). The Mesozoic-Cenozoic East China rift system. *Tectonophysics*, 208, 341-363.

VanDecar, J. C., & Crosson, R. S. (1990). Determination of teleseismic relative phase arrival times using multi-channel cross-correlation and least squares. *Bulletin of the Seismological Society of America*, 80, 150-169.

Waldhauser, F., Lippitsch, R., Kissling, E., & Ansorge, J. (2002). High-resolution teleseismic tomography of upper-mantle structure using an a priori three-dimensional crustal model. *Geophysical Journal International*, 150, 403-414.

Wang, F., Zhou, X., Zhang, L., Ying, J., Zhang, Y., Wu, F., & Zhu, R. (2006). Late Mesozoic volcanism in the Great Xing'an Range (NE China): timing and implications for the dynamic setting of NE Asia. *Earth and Planetary Science Letters*, 251, 179-198.

Wang, X., Wilde, S. A., Li, Q., & Yang, Y. (2015). Continental flood basalts derived from the hydrous mantle transition zone. *Nature Communications*, 6, https://doi: 10.1038/ncomms8700.

Wang, X., Chen, L., Hofmann, A. W., Mao, F., Liu, J., Zhong, Y., Xie, L., & Yang, Y. (2017). Mantle transition zone-derived EM1 component beneath NE China: Geochemical evidence from Cenozoic potassic basalts. *Earth and Planetary Science Letters*, 465, 16-28.

Wei, W., Xu, J., Zhao, D., & Shi, Y. (2012). East Asia mantle tomography: New insight into plate subduction and intraplate volcanism. *Journal of Asian Earth Sciences*, 60, 88-103.

Wei, W., Zhao, D., & Xu, J. (2013). P-wave anisotropic tomography in Southeast Tibet: New insight into the lower crustal flow and seismotectonics. *Physics of the Earth and Planetary Interiors*, 222, 47-57.

Wei, W., Zhao, D., Xu, J., Wei, F., & Liu, G. (2015). P and S wave tomography and anisotropy in Northwest Pacific and East Asia: constraints on stagnant slab and intraplate volcanism. *Journal of Geophysical Research: Solid Earth*, 120, 1642-1666.

Wessel, P., Smith, W., Scharroo, R., Luis, J., & Wobbe, F. (2013), Generic mapping tools: Improved version released, Eos Transactions, American Geophysical Union, 94, 409–410.

Wu, F., Lin, J., Wilde, S. A., Zhang, X. O., & Yang, J. (2005). Nature and significance of the Early Cretaceous giant igneous event in eastern China. *Earth and Planetary Science Letters*, 233, 103-119.

Xiao, W., Windley, B. F., Hao, J., & Zhai, M. (2003). Accretion leading to collision and the Permian Solonker suture, Inner Mongolia, China: termination of the central Asian orogenic belt. *Tectonics*, 22, doi: 10.1029/2002TC001484.

Xu, Y., Zhang, H., Qiu, H., Ge, W., & Wu, F. (2012). Oceanic crust components in continental basalts from Shuangliao, Northeast China: Derived from the mantle transition zone?. *Chemical Geology*, 328, 168-184.

Zhang F., Wu, Q., & Li, Y. (2013a). The traveltime tomography study by teleseismic P wave data in the Northeast China area. *Chinese Journal of Geophysics*, 56, 2690-2700 (in Chinese with English abstract).

Zhang, F., Wu, Q., Grand, S. P., Li, Y., Gao, M., Demberel, S., Ulziibat, M., & Sukhbaatar, U. (2017). Seismic velocity variations beneath central Mongolia: Evidence for upper mantle plumes?. *Earth and Planetary Science Letters*, 459, 406-416.

Zhang, G., Wu, Q., Pan, J., Zhang, F., & Yu, D. (2013b). Study of crustal structure and Possion ration of NE China by H-K stack and CCP stack methods. *Chinese Journal of Geophysics*, 56, 4084-4094 (in Chinese with English abstract).

Zhang, J., Gao, S., Ge, W., Wu, F., Yang, J., Wilde, S. A., & Li, M. (2010). Geochronology of the Mesozoic volcanic rocks in the Great Xing'an Range, northeastern China: implications for subduction-induced delamination. *Chemical Geology*, 276, 144-165.

Zhang, M., Suddaby, P., Thompson, R. N., Thirlwall, M. F., Menzies, M. A., 1995. Potassic volcanic rocks in NE China: geochemical constraints on mantle source and magma genesis. *Journal of Petrology*, 36, 1275-1303.

Zhang, M., Zhou, X., & Zhang, J. (1998). Nature of the lithospheric mantle beneath NE China: evidence from potassic volcanic rocks and mantle xenoliths. In: Flower, M.F.J., Chung, S. L., Lo, C. H., Lee, T. Y. (Eds.), *Mantle Dynamics and Plate Interactions in East Asia*, American Geophysical Union, Geodynamics Series, vol. 27, pp. 197 – 219.

Zhang, R., Wu, Q., Sun, L., He, J., & Gao, Z. (2014). Crustal and lithospheric structure of Northeast China from S-wave receiver functions. *Earth and Planetary Science Letters*, 401, 196-205.

Zhao, D. (2004). Global tomographic images of mantle plumes and subducting slabs: insight into deep Earth dynamics. *Physics of the Earth and Planetary Interiors*, 146, 3-34.

Zhao, D., Hasegawa, A., & Horiuchi, S. (1992). Tomographic imaging of P and S wave velocity structure beneath northeastern Japan. *Journal of Geophysical Research: Solid Earth*, 97, 19909-19928.

Zhao, D., Hasegawa, A., & Kanamori, H. (1994). Deep structure of Japan subduction zone as derived from local, regional, and teleseismic events. *Journal of Geophysical Research*, 99, 22313-22329.

Zhao, D., & Tian, Y. (2013). Changbai intraplate volcanism and deep earthquakes in East Asia: a possible link?. *Geophysical Journal International*, 195, 706-724.

Zhao, D., Tian, Y., Lei, J., Liu, L., & Zheng, S. (2009). Seismic image and origin of the Changbai intraplate volcano in East Asia: role of big mantle wedge above the stagnant Pacific slab. *Physics of the Earth and Planetary Interiors*, 173, 197-206.

Zhao, D., Yanada, T., Hasegawa, A., Umino, N., & Wei, W. (2012). Imaging the subducting slabs and mantle upwelling under the Japan Island. *Geophysical Journal International*, 190, 816-828.

Zhao, D., Yamamoto, Y., & Yanada, T. (2013). Global mantle heterogeneity and its influence on teleseismic regional tomography. *Gondwana Research*, 23, 595-616.

Zhao, Y. W., & Fan, Q. C. (2012). Mantle sources and magma genesis of Quaternary volcanic rocks in the Halaha river and Chaoer river area, Great Xing'an Range. *Acta Petrologica Sinica*, 28, 1119 – 1129 (in Chinese with English abstract).

Zou, H., Reid, M. R., Liu, Y., Yao, Y., Xu, X., & Fan, Q. (2003). Constraints on the origin of historic potassic basalts from northeast China by U-Th disequilibrium data. *Chemical Geology*, 200, 189-201.

Figure captions

Figure 1. A map showing the regional tectonics and topographic relief in northeast China and adjacent areas. The purple areas show the Cenozoic volcanic rocks, the red triangles show the Holocene volcanoes, and the dashed lines show the major faults. In the inset map, the blue rectangle shows the present study region and the green broken curves denote the isodepth contours of the subducting Pacific plate.

Figure 2. Distribution of seismic stations (purple stars) along the EH and SM profiles used in the study. The data are from ChinArray (ChinArray, 2006). The red triangles denote the Holocene volcanoes, and the dashed lines show the major faults. In the inset map, the green dots denote the teleseismic events that yielded P-wave relative arrival times used in the tomographic inversions, the blue lines denote the major plate boundaries, and the three concentric circles denote epicentral distances of 30, 60 and 90 degrees.

Figure 3. Distribution of P-wave ray paths along the (a) EH and (b) SM profiles after the crustal correction. The red and blue lines show the rays with delayed and early

arrivals, respectively. The mean relative travel-time residuals (RTT) at every station (green stars) are shown at the top, where the red circles and blue diamonds denote delayed and early arrivals respectively. The scales for the RTT residuals are shown at the bottom.

Figure 4. The trade-off curves between velocity perturbation variance and data variance reduction for tomographic inversions with varying damping and smoothing values for the (left) EH and (right) SM profiles. The dot with the black circle shows the optimal damping value.

Figure 5. Histograms of relative P-wave travel-time (RTT) residuals (a, b) before and (c, d) after tomographic inversions for the (a, c) EH and (b, d) SM profiles.

Figure 6. A discrete spike test. The input spherical anomalies have a diameter of 100 km. The recovered P-wave models are shown at four depth slices (100, 300, 500 and 700 km) and along a vertical cross-section that is located near the EH line. The red triangle denotes the Wudalianchi volcano. The two white dashed lines in the vertical cross-sections denote the 410 and 660 km discontinuities. The velocity perturbation scale is shown at the bottom.

Figure 7. The same as Figure 6 but for a discrete spike test along the SM profile. The red triangle denotes the Halaha volcano.

Figure 8. Map views of the P-wave tomographic model along the EH profile. The layer depth is shown at the upper-right corner of each map. Red and blue colors show slow and fast velocity perturbations respectively, whose scale is shown at the bottom. The red triangle denotes the Wudalianchi volcano.

Figure 9. The same as Figure 8 but for P-wave tomography along the SM profile. The red triangle denotes the Halaha volcano.

Figure 10. Vertical cross-sections of P-wave tomography along the (a) EH and (b) SM lines. Red and blue colors denote slow and fast velocity perturbations, respectively, whose scale is shown at the bottom. The red triangles denote the Wudalianchi volcano (a) and the Halaha volcano (b). The surface topography (black line) and seismic stations (green stars) are shown above the cross-sections. The distance between the adjacent white dots at the top is 1° (~110 km). The two white dashed lines denote the 410 and 660 km discontinuities.

Figure 11. Results of synthetic resolution tests. The left and right panels show the input synthetic models and the recovered models after tomographic inversion, respectively.

Figure 12. A cartoon showing the main features of the upper-mantle structure and mechanisms driving intraplate volcanism in Northeast China. See the text for details.

Figure 1.

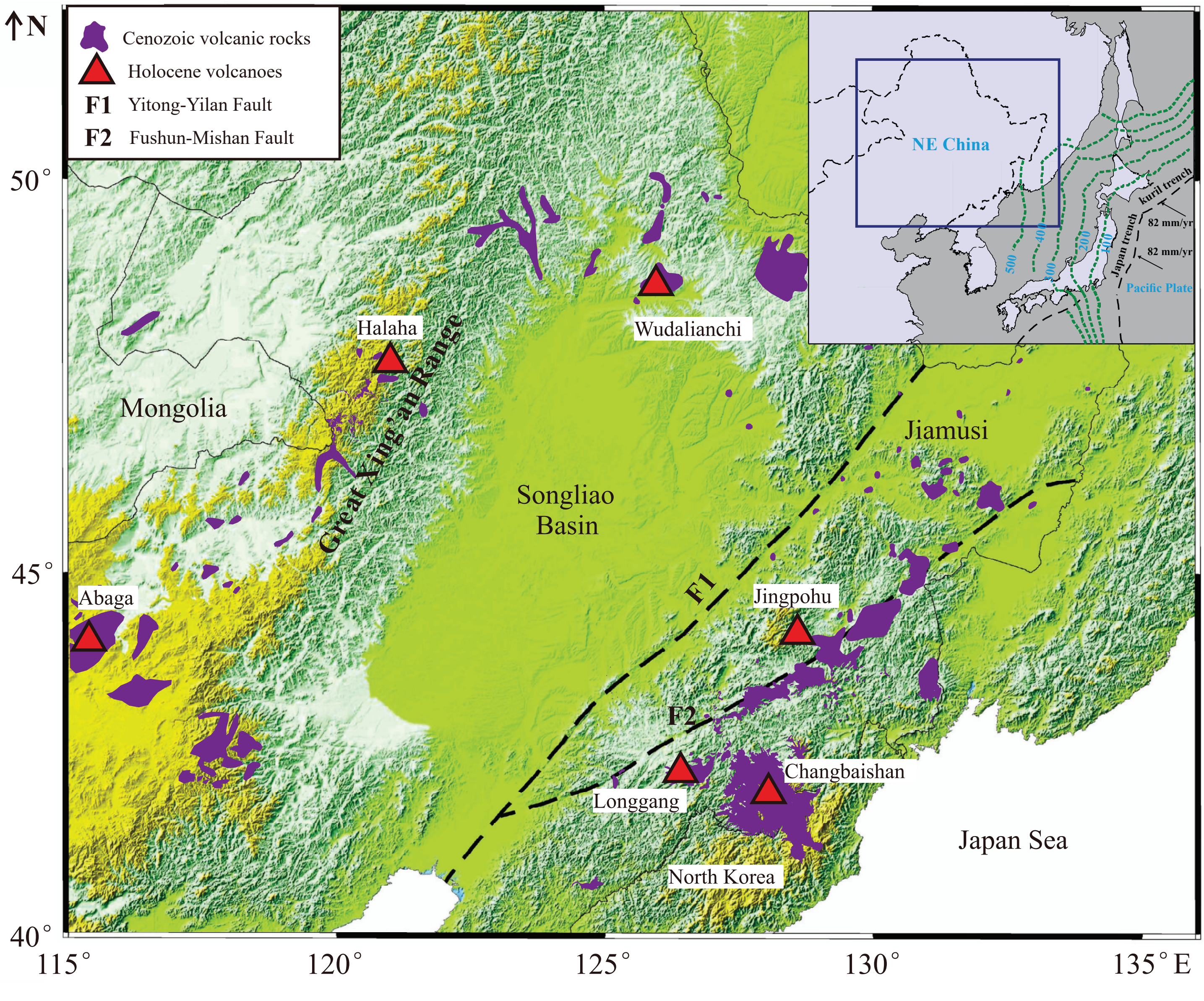

N
Cenozoic volcanic rocks
Holocene volcanoes
F1 Yitong-Yilan Fault
F2 Fushun-Mishan Fault
NE China
500
400
300
200
100
kuril trench
Japan trench
82 mm/yr
82 mm/yr
Pacific Plate
Halaha
Wudalianchi
Great Xing'an Range
Mongolia
Jiamusi
Songliao Basin
F1
F2
Abaga
Jingpohu
Longgang
Changbaishan
North Korea
Japan Sea
50°
45°
40°
115°
120°
125°
130°
135°E

Figure 2.

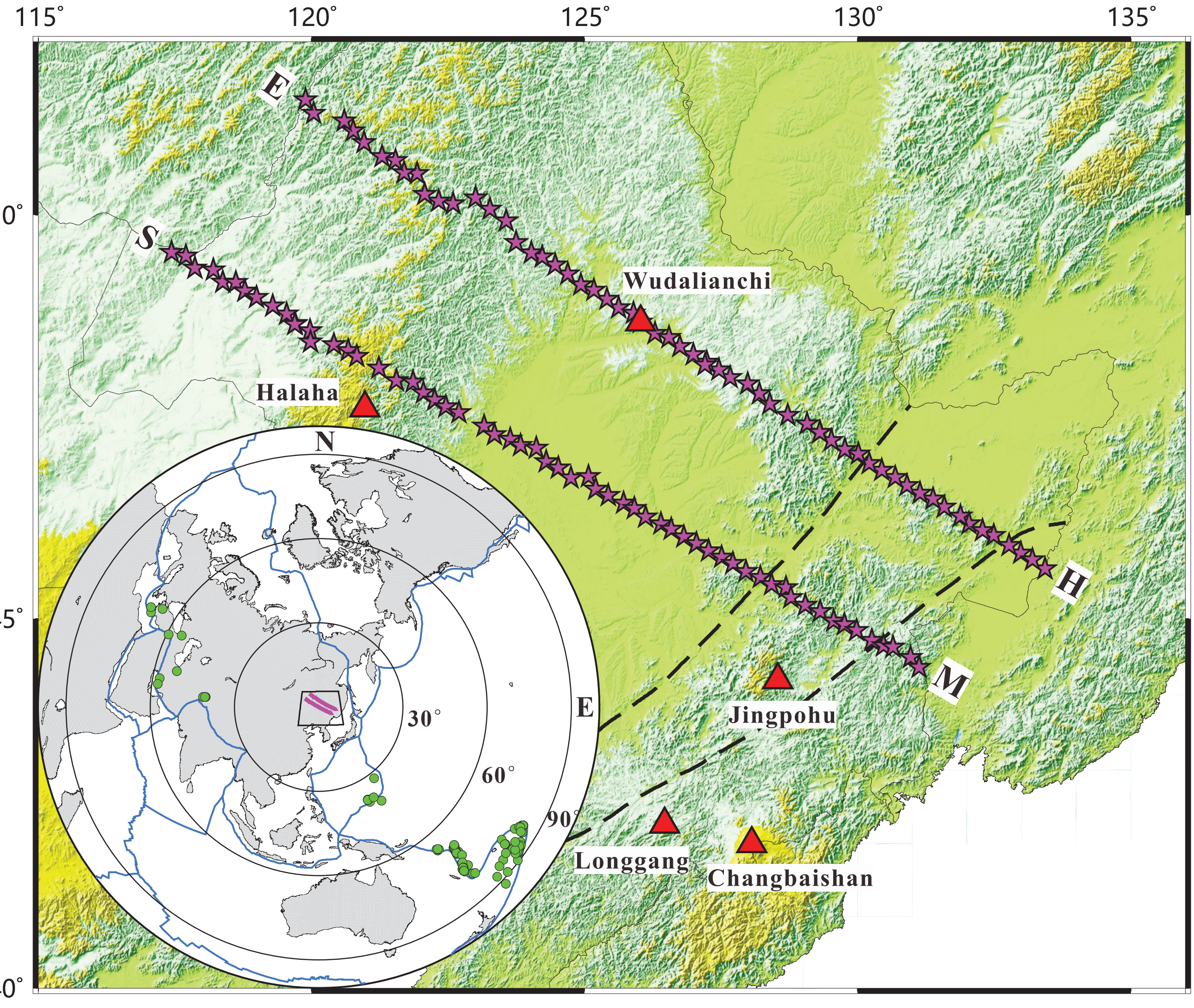

115°
120°
125°
130°
135°
50°
45°
40°
E
S
H
M
Wudalianchi
Halaha
Jingpohu
Longgang
Changbaishan
N
E
30°
60°
90°

Figure 3.

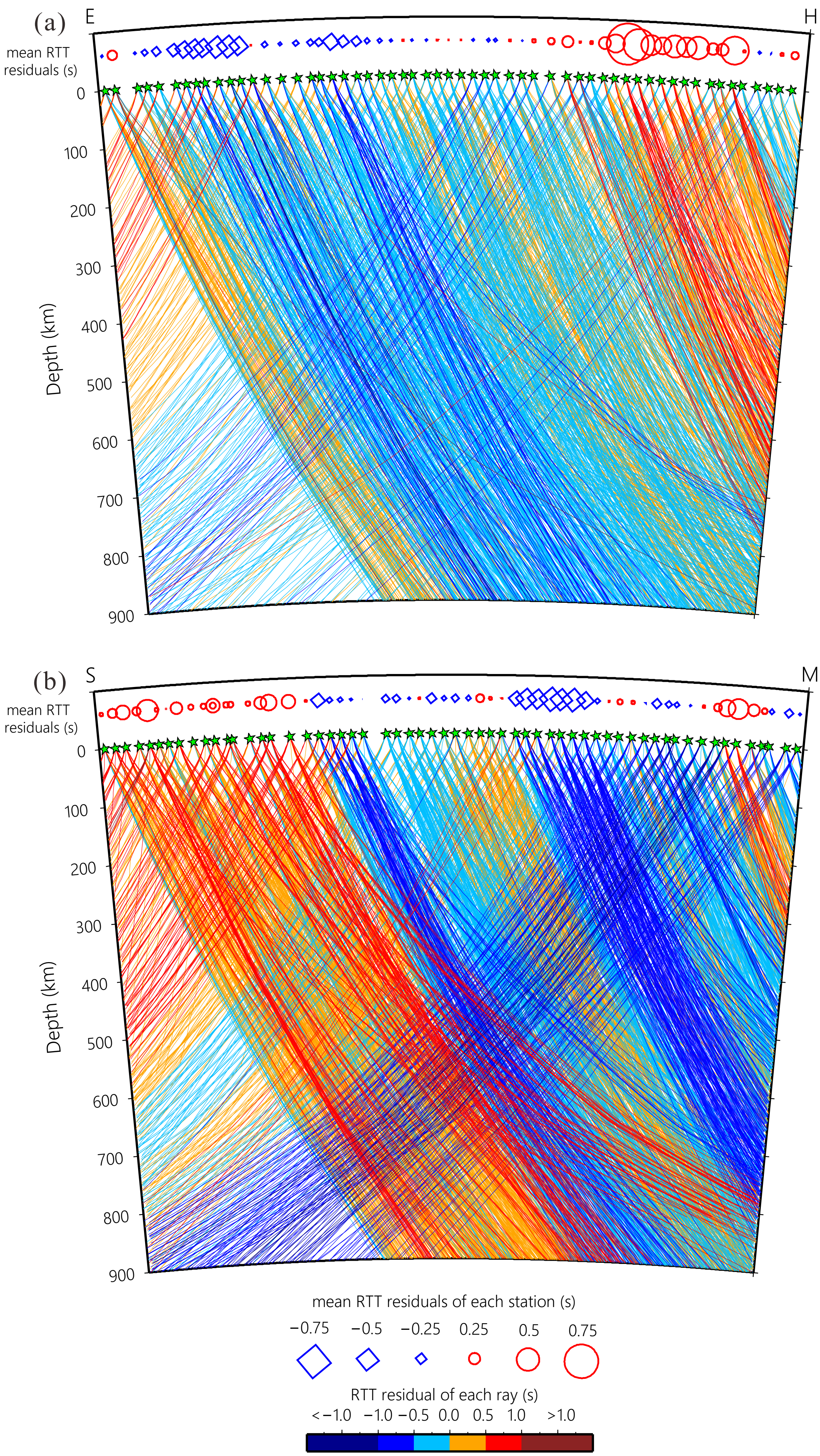
(a)
E
H
mean RTT residuals (s)
Depth (km)
0
100
200
300
400
500
600
700
800
900
(b)
S
M
mean RTT residuals (s)
Depth (km)
0
100
200
300
400
500
600
700
800
900
mean RTT residuals of each station (s)
−0.75 −0.5 −0.25 0.25 0.5 0.75
RTT residual of each ray (s)
<−1.0 −1.0 −0.5 0.0 0.5 1.0 >1.0

Figure 4.

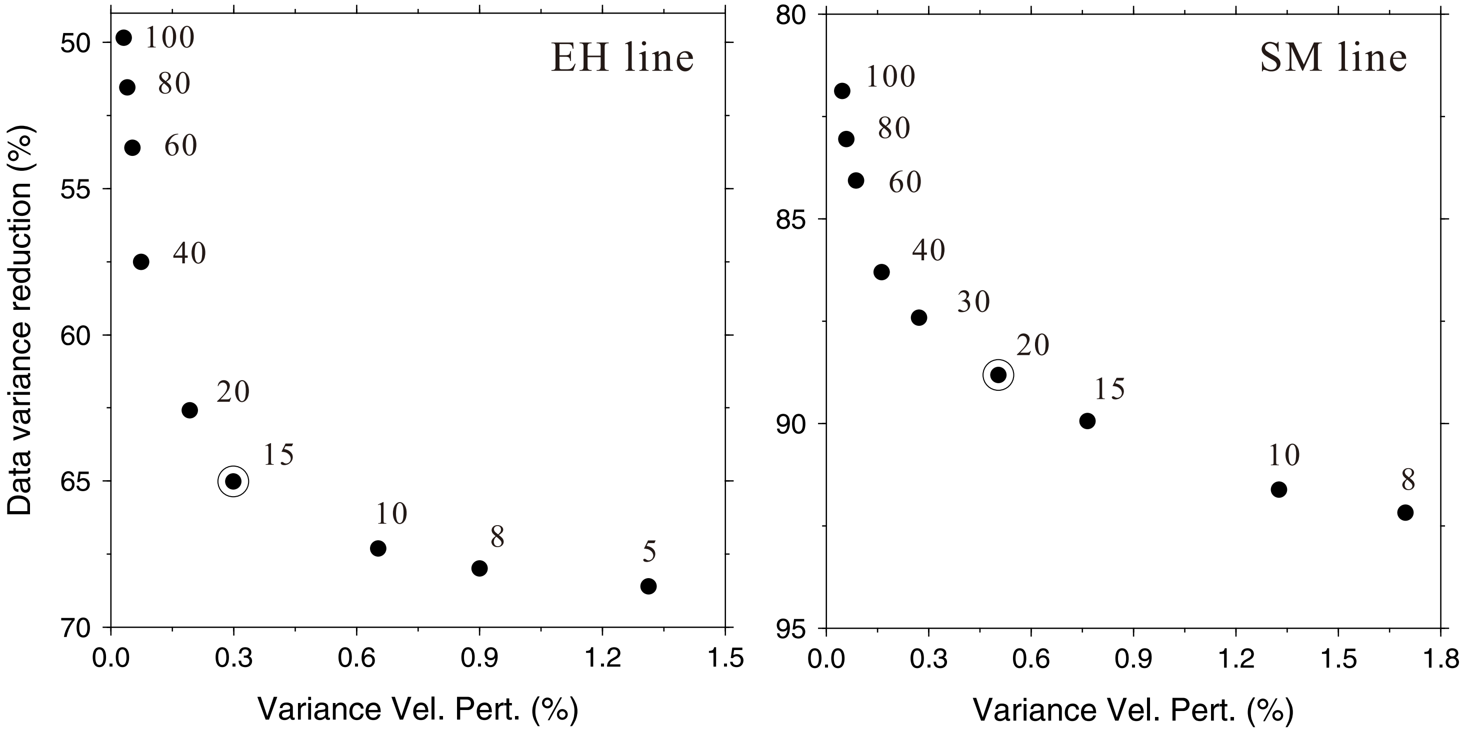
EH line
SM line
Data variance reduction (%)
Variance Vel. Pert. (%)
Variance Vel. Pert. (%)
100
80
60
40
20
15
10
8
5
100
80
60
40
30
20
15
10
8
50
55
60
65
70
0.0
0.3
0.6
0.9
1.2
1.5
80
85
90
95
0.0
0.3
0.6
0.9
1.2
1.5
1.8

Figure 5.

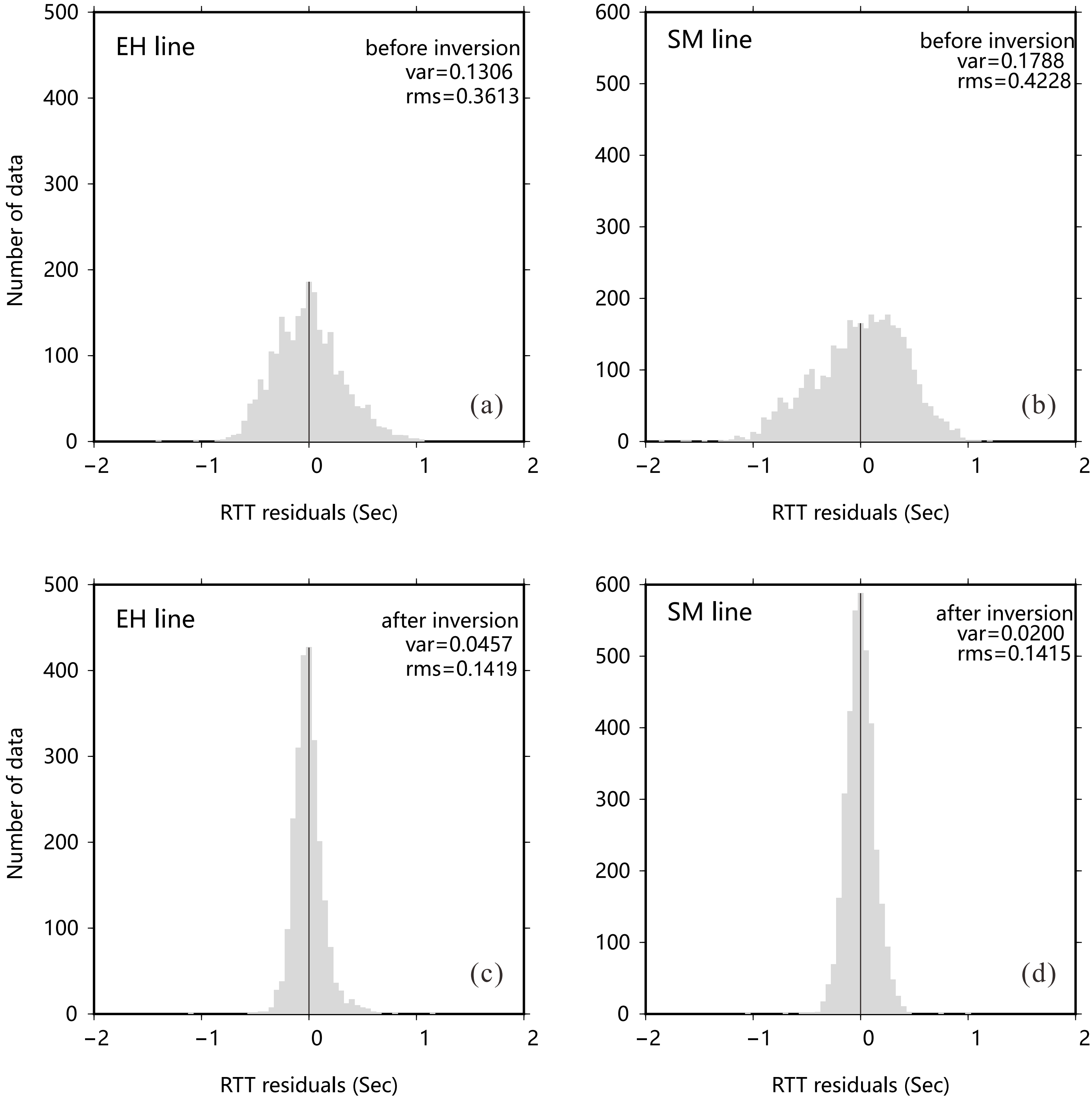
EH line
before inversion
var=0.1306
rms=0.3613
Number of data
RTT residuals (Sec)
(a)
SM line
before inversion
var=0.1788
rms=0.4228
RTT residuals (Sec)
(b)
EH line
after inversion
var=0.0457
rms=0.1419
Number of data
RTT residuals (Sec)
(c)
SM line
after inversion
var=0.0200
rms=0.1415
RTT residuals (Sec)
(d)

Figure 6.

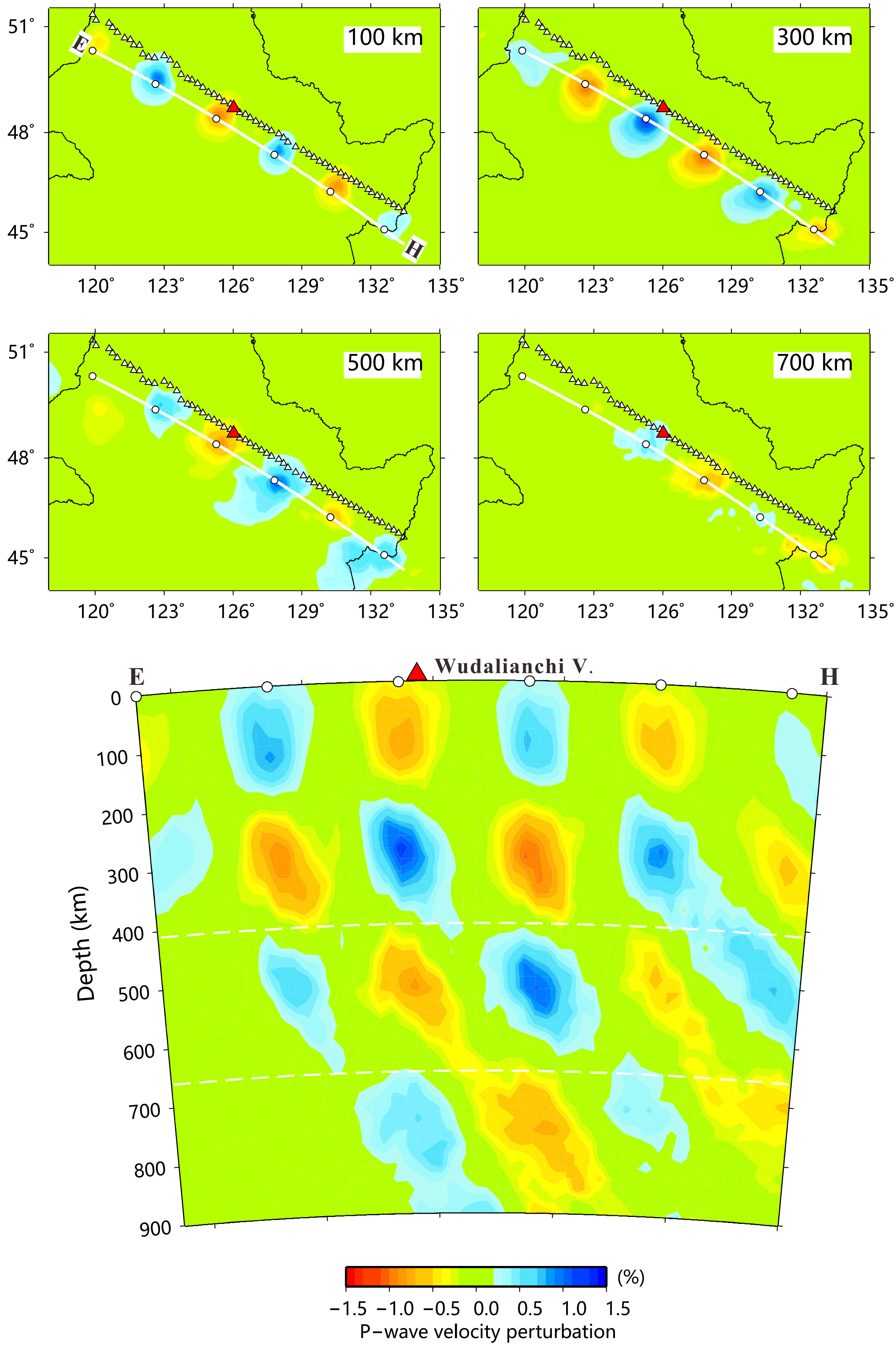
100 km
300 km
500 km
700 km
E
H
51°
48°
45°
120°
123°
126°
129°
132°
135°
Wudalianchi V.
Depth (km)
0
100
200
300
400
500
600
700
800
900
(%)
−1.5 −1.0 −0.5 0.0 0.5 1.0 1.5
P−wave velocity perturbation

Figure 7.

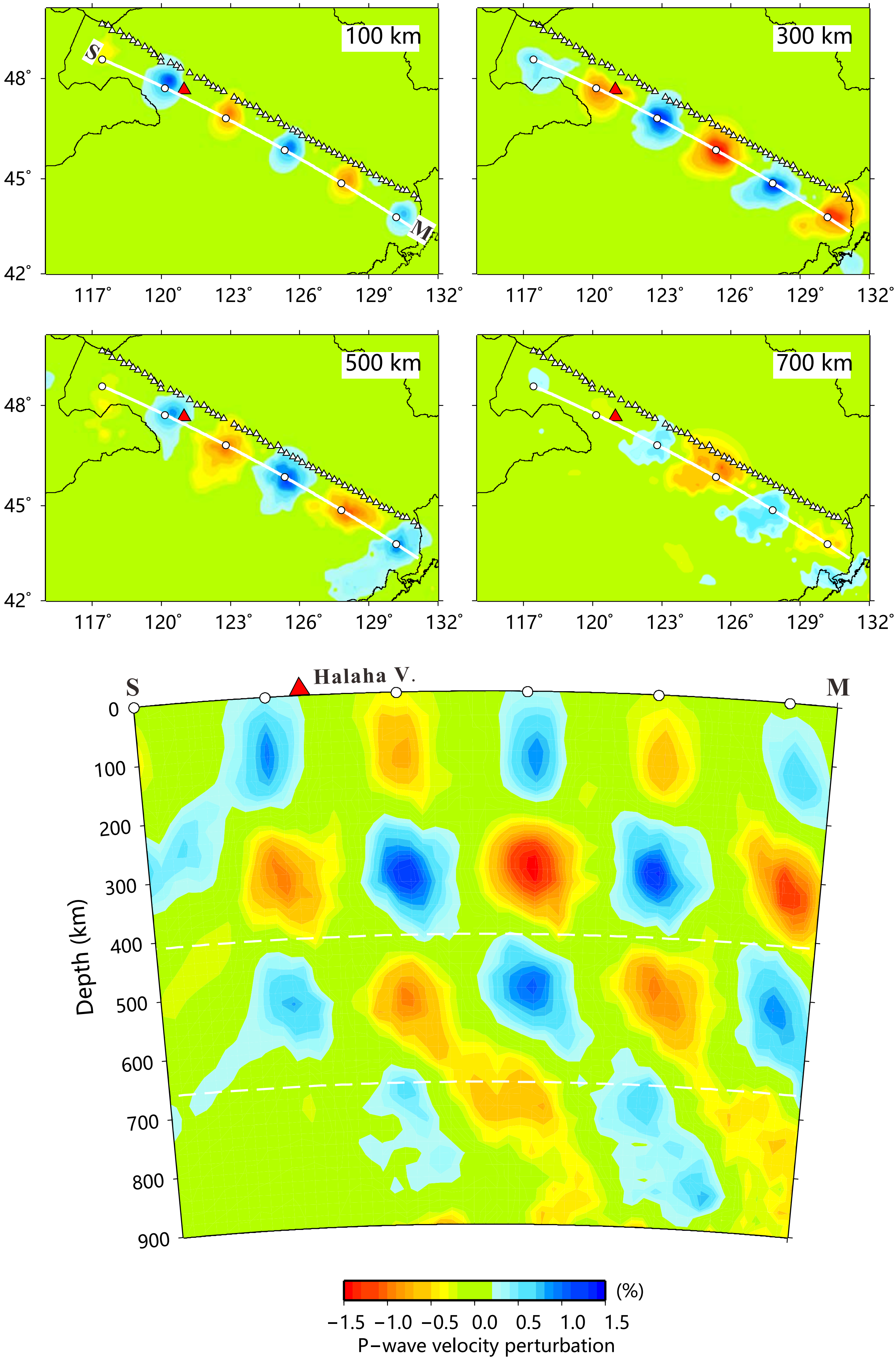
100 km
300 km
500 km
700 km
S
M
48°
45°
42°
117°
120°
123°
126°
129°
132°
Halaha V.
Depth (km)
0
100
200
300
400
500
600
700
800
900
(%)
−1.5 −1.0 −0.5 0.0 0.5 1.0 1.5
P−wave velocity perturbation

Figure 8.

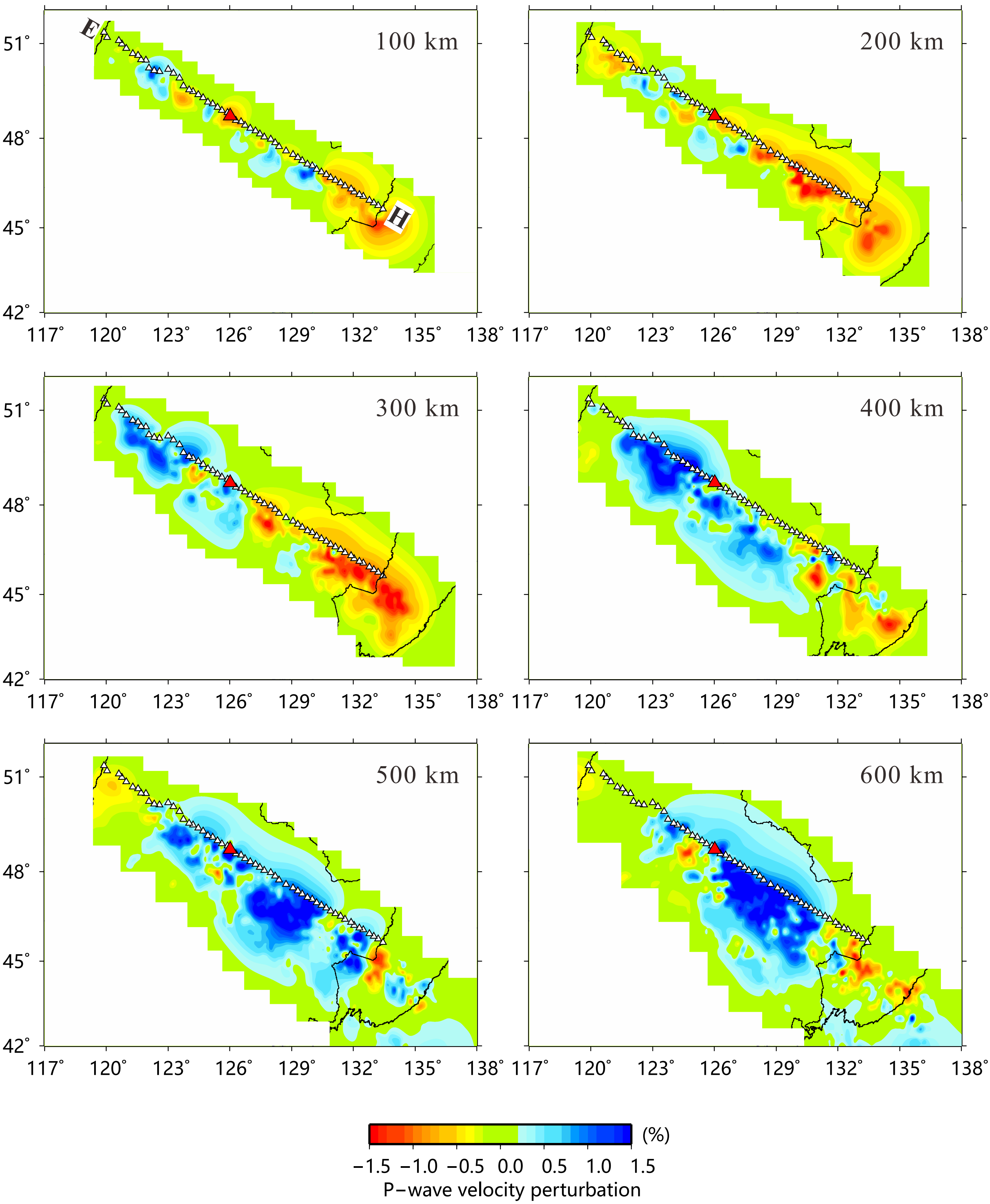

100 km
200 km
300 km
400 km
500 km
600 km
E
H
51°
48°
45°
42°
117°
120°
123°
126°
129°
132°
135°
138°
(%)
−1.5 −1.0 −0.5 0.0 0.5 1.0 1.5
P−wave velocity perturbation

Figure 9.

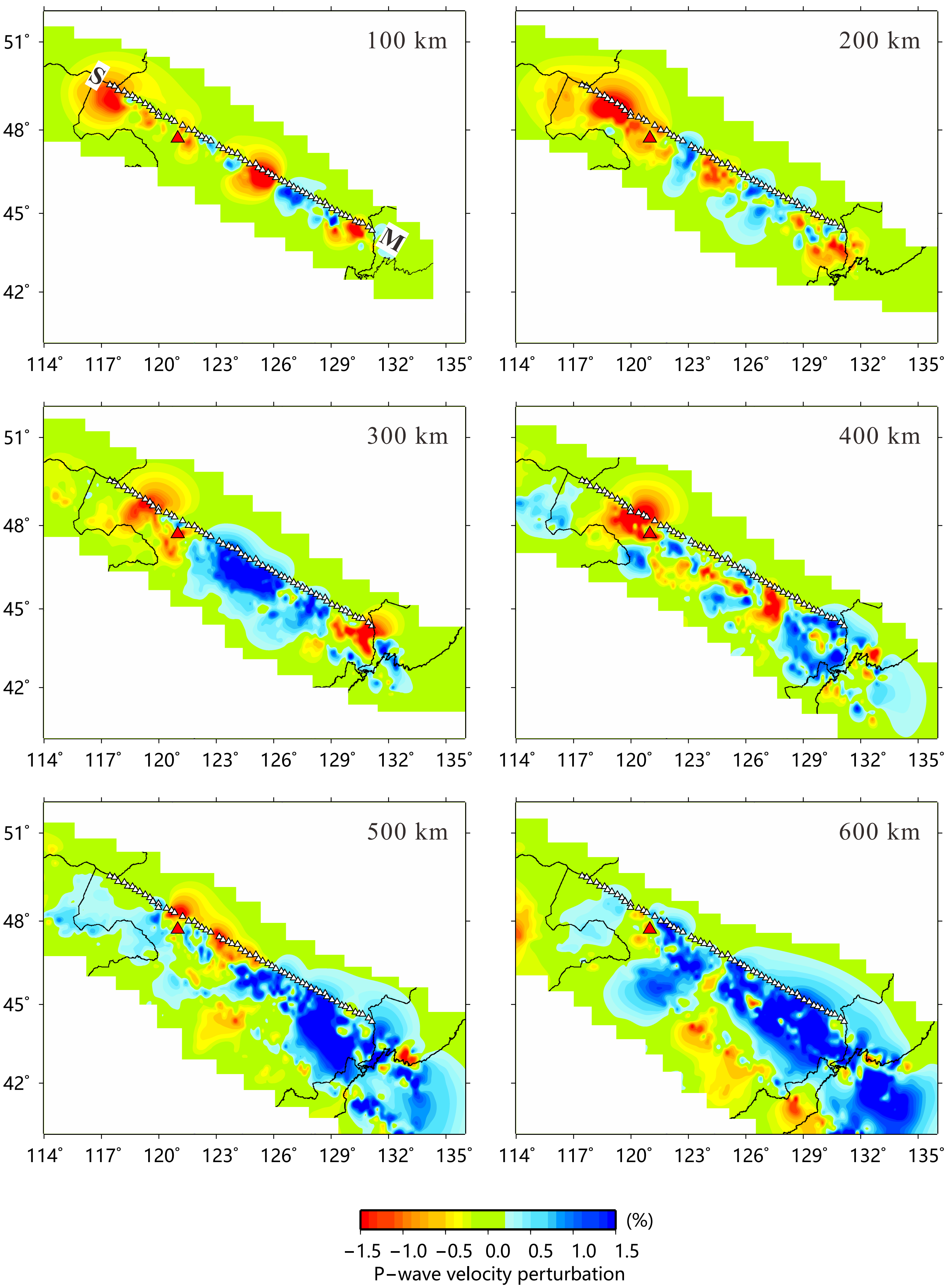
100 km
200 km
300 km
400 km
500 km
600 km
S
M
51°
48°
45°
42°
114°
117°
120°
123°
126°
129°
132°
135°
(%)
−1.5 −1.0 −0.5 0.0 0.5 1.0 1.5
P−wave velocity perturbation

Figure 10.

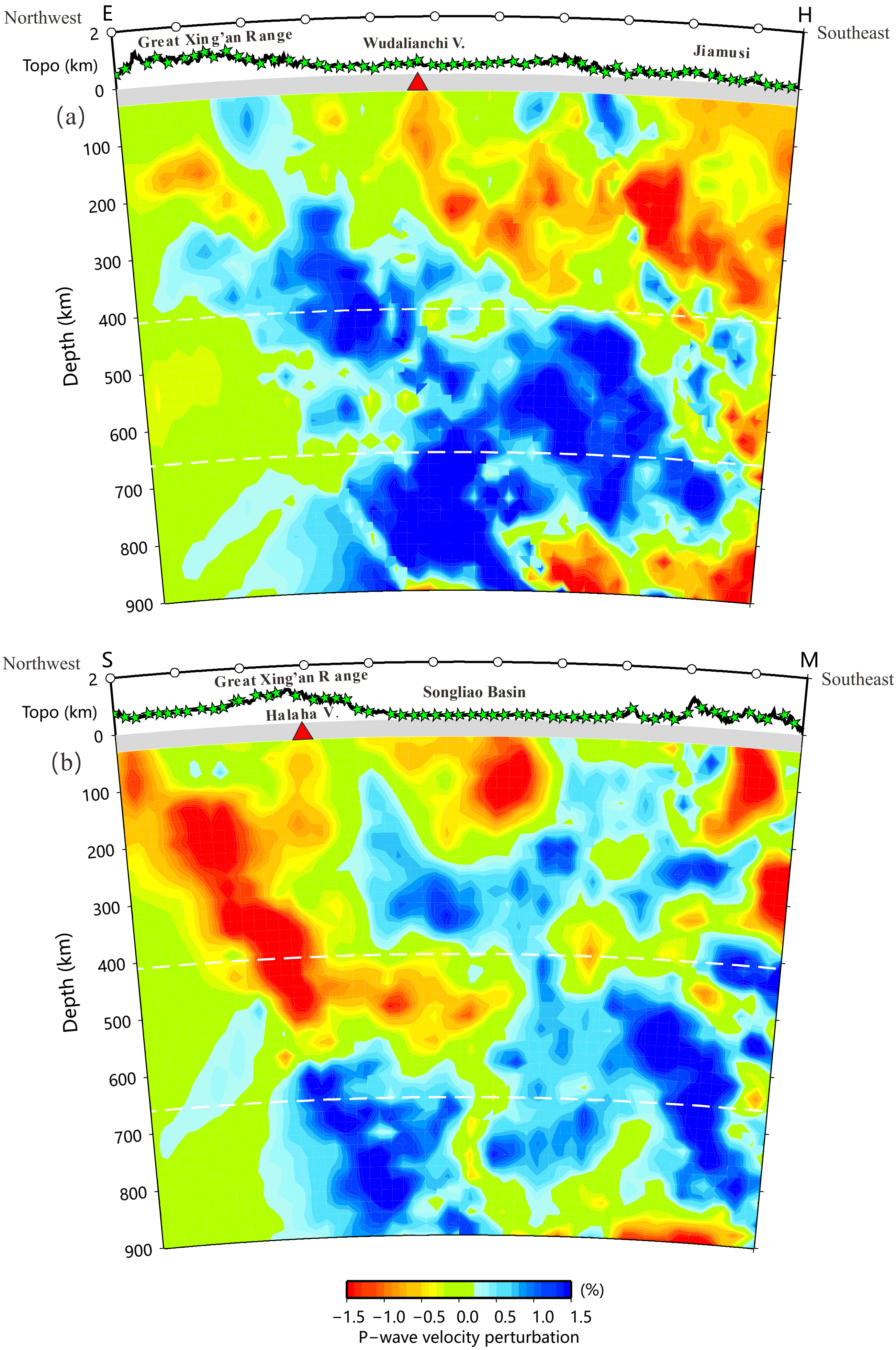
Northwest
E
H
Southeast
Topo (km)
Great Xing'an Range
Wudalianchi V.
Jiamusi
(a)
Depth (km)
0
100
200
300
400
500
600
700
800
900
Northwest
S
M
Southeast
Topo (km)
Great Xing'an R ange
Halaha V.
Songliao Basin
(b)
Depth (km)
(%)
−1.5 −1.0 −0.5 0.0 0.5 1.0 1.5
P−wave velocity perturbation

Figure 11.

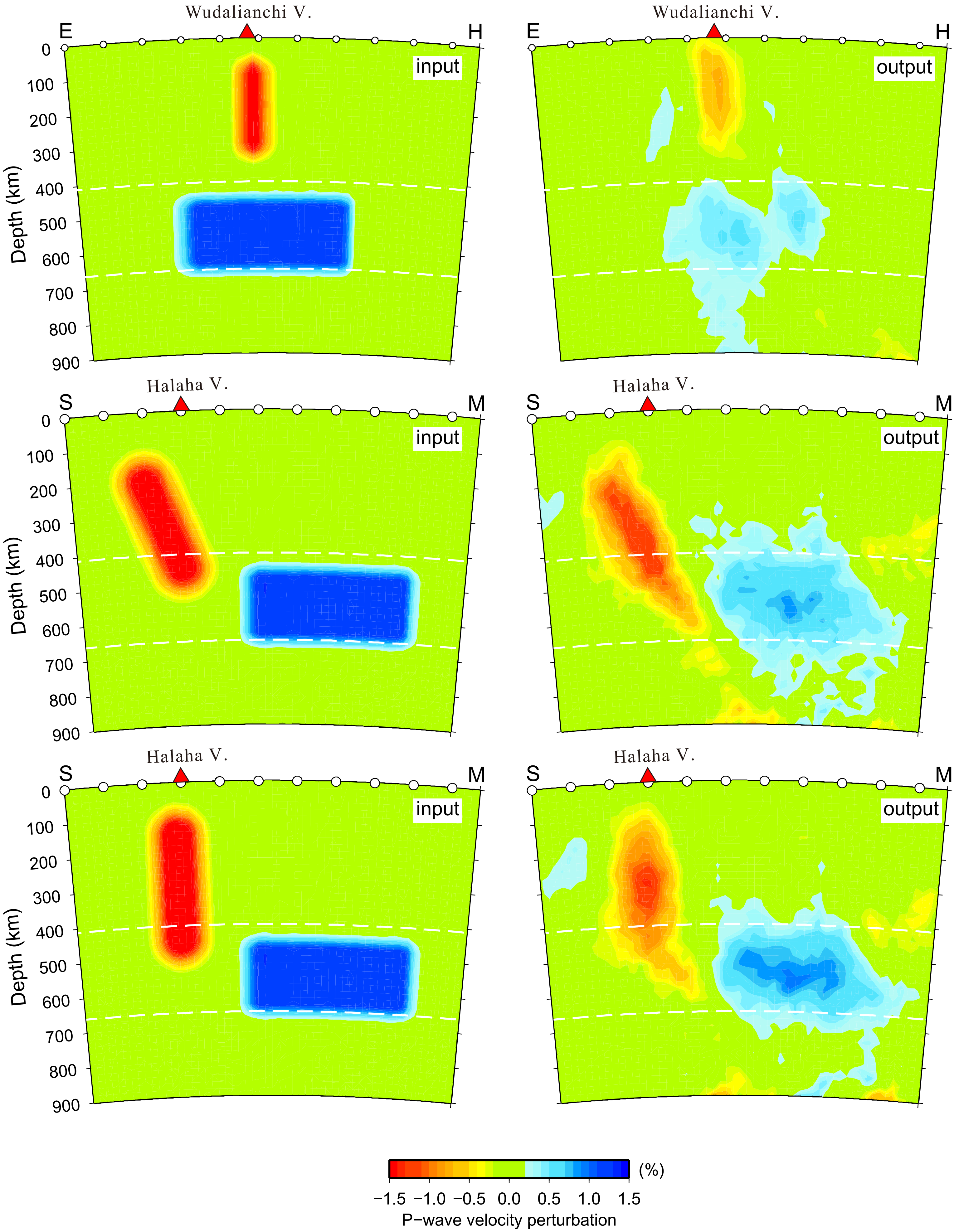
Wudalianchi V.
E
H
input
output
Depth (km)
0
100
200
300
400
500
600
700
800
900
Halaha V.
S
M
(%)
−1.5 −1.0 −0.5 0.0 0.5 1.0 1.5
P−wave velocity perturbation

Figure 12.

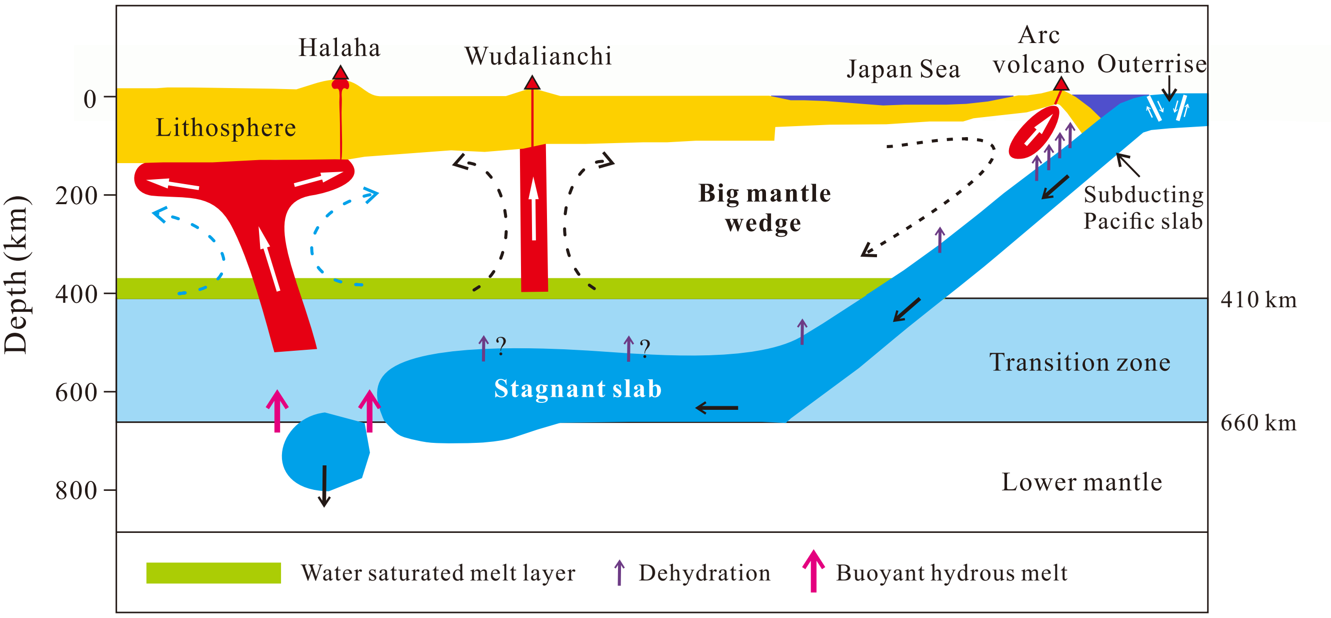

Halaha
Wudalianchi
Japan Sea
Arc volcano
Outerrise
0
200
400
600
800
Depth (km)
Lithosphere
Big mantle wedge
Subducting Pacific slab
410 km
Transition zone
Stagnant slab
660 km
Lower mantle
?
?
Water saturated melt layer
Dehydration
Buoyant hydrous melt

–